Microstructure and Dynamics of Nanocellulose Films: Insights into the Deformational Behavior

Zhaofan Li [1], Yangchao Liao [1], Yao Zhang [2], Yida Zhang [3], Wenjie Xia [1,4]*

[1]Department of Civil, Construction and Environmental Engineering, North Dakota State University, Fargo, ND 58108, United States

[2]Department of Mechanics, School of Aerospace Engineering, Huazhong University of Science and Technology, Wuhan, 430074, China

[3]University of Colorado Boulder, Department of Civil, Environmental and Architectural Engineering, Boulder, CO 80309, United states

[4]Materials and Nanotechnology, North Dakota State University, Fargo, ND 58108, United States

*To whom correspondence should be addressed.

Contact information: wenjie.xia@ndsu.edu

ABSTRACT

Cellulose nanocrystals (CNCs) thin films draw considerable interest in engineering and technological applications due to their excellent mechanical and physical properties associated with dynamic and microstructural features. Here, we employ coarse-grained molecular dynamics (CG-MD) simulations to investigate how the dynamics and microstructure change in the CNC films under tensile deformation. Our results show that the Young's modulus can be quantitatively predicted by the power-law scaling relationship with initial packing density, where higher density leads to an increase in both modulus and strength. By evaluating the molecular local stiffness during the tensile process, our findings show that CNC film with higher density exhibits a higher degree of dynamic heterogeneity, which is greatly reduced under deformation. Our results further demonstrate that randomly oriented CNCs tend to be more aligned with the tensile direction associated with higher free volume and porosity during the deformation; however, the dynamics of CNC is more associated with the degree of local packing and density rather than the CNC orientation. Our study provides fundamental insights into deformational mechanisms associated with the microstructure and dynamics of CNC films at a molecular level, aiding in the tailored design of cellulose-based materials for their mechanical performance.

INTRODUCTION

With the increasing demands in multifunctionality, recyclability, and environmental friendliness [1,2], cellulose-based nanomaterials have drawn considerable attentions as sustainable and renewable materials that offer potential alternatives to conventional petroleum-derived polymers in various applications, such as nanocomposites [3,4], advanced manufacturing [5,6], electronics [7], tissue engineering [8,9], and food packaging [10,11]. As the most abundant biopolymer on earth, a cellulose chain typically has a high molecular weight consisting of glucose repeat units; multiple cellulose chains can stack together to form a hierarchical paracrystalline structure, which can be extracted from a wide range of biological sources (*e.g.*, wood, plant, bacterial, algae, and tunicates) [12–16]. Cellulose can be further chemically or mechanically processed in the form of cellulose nanocrystals (CNCs) or nanofibers (CNFs) [17–20], which exhibit remarkable mechanical properties due to rich interchain/intrachain hydrogen-bonding. In particular, CNCs exhibit a rod-like shape with a high aspect ratio (*i.e.*, 3–5 nm in cross section dimensions, 50–500 nm in length) and possess stiff and predominantly crystalline structures after removal of amorphous domains, achieving remarkably high strength and stiffness (*i.e.*, comparable to structural steel) [15]. These exceptional features have rendered CNCs as ideal candidates of nanoscale building blocks for the development of structural materials [21–23].

Recently, there is a particular upsurge of interests in nanocellulose-based thin films [24–26] comprised of readily self-assembled CNCs/CNFs, forming the so-called cellulose nanopapers. These cellulose thin films or nanopapers have been produced by several approaches, such as spin coating [27], Langmuir–Schaeffer [28], and Langmuir–Blodgett technique [29]. Cellulose nanofibers are often randomly distributed in ordinary nanopapers, exhibiting strong network-forming characteristics [30], yielding interesting physical properties including optical transparency

[31], low thermal expansion [24], high porosity and permeability, in addition to excellent structural performance [32]. For instance, light-weight porous nanocellulose derivative foams, exhibiting high specific surface area and high ductility and toughness, have received a great deal of attention and are of interest for applications involving mechanical energy absorption and sound insulation [32]. The full potential of nanopapers, however, is difficult to control due to their complex microstructural features arising from the random orientation of CNFs/CNCs. Considerable efforts have been made towards this direction. For instance, CNCs within suspensions can be oriented in a given direction by applying external force with multiple experimental techniques, including electric [33,34], magnetic fields [35,36], and shear casting [35,36]. The internal structure of processed CNC nanopapers can also adopt various other architectures, such as highly aligned, brick-and-mortar type, Bouligand (or twisted plywood) microstructures [37,38]. as well as isotropic assemblies, chiral nematic ordering fashion [39,40]. Moreover, it has been shown that the mechanical, barrier properties, and impact tolerance are highly dependent upon the microstructural arrangements (*e.g.*, nanofiber orientation) of CNC thin films [30,37,41,42]. In particular, homogeneous dispersion of CNCs forming random network yields overall isotropy of physical and mechanical properties, and the porosity and density can be readily varied to achieve tunable permeability usage and lightweight performance. Despite considerable efforts, it still remains largely elusive that how the microstructural features (*e.g.*, density, nanocrystal orientation) impact the dynamics and deformational response for describing structure-property relationship of cellulose nanopapers having a network topology.

To uncover the underlying molecular mechanisms associated with mechanical properties of nanocellulose films, several microstructure-based modeling approaches have been developed to interpret the mechanical behavior of materials and guide the design. Fibrous network model based

on finite element method (FEM) has been useful in predicting the elastic modulus of cellulose nanopaper and elucidating the effect of inter-fiber bonds density and bonds stiffness on the modulus [43,44]. Moreover, Meng *et al.* developed a theoretical crack-bridging model to investigate the alignment effect on the fracture toughness of cellulose nanopaper [45]. Despite the success of continuum and theoretical modeling, they may lack of preserving nanoscopic details necessary to accurately capture the mechanical performance of nanocellulose films. Molecular dynamics (MD) simulations have been proved to be highly useful in this regard. All-atomistic (AA) MD simulations have been extensively employed to accurately present the nanoscale deformation and failure behavior of CNCs [46–49]. Zhu *et al.* proposed a molecular chain pull-out model to reveal the hydrogen bond breaking and re-forming mechanism, which in turn dictate the enhanced energy dissipation during sliding [50]. More recently, coarse-grained (CG) MD simulations have gained tremendous popularity due to its access to larger spatiotemporal scale as well as providing avenues for parametric studies. These methods have been successfully applied to CNC materials, both during quasi-static [40,51–53] and dynamic deformation procedures [37]. For instance, a CG model proposed by Shishehbor and Zavattieri offers a promising scheme to capture mechanical and interfacial features of CNC-based materials [54]. Ray *et al.* recently establish a bottom-up CG modeling which is capable of modeling cellulose fibers ranging from nanometers to microns and studying the deformation process of a cellulose nanopaper [55].

In this work, we aim to better understand the dynamics and mechanical performance of nanocellulose thin films consisting of randomly oriented CNCs. By employing an atomistically-informed CG model developed for CNCs [40], we systematically explore the microstructural features of CNCs (*i.e.*, density, porosity, and nanocrystal orientation) and their coupling with the dynamics and mechanical properties of a random network of CNC nanopaper under tensile

deformation. Specifically, first, the mechanical properties of CNC film with various packing density are compared to investigate the relationship between density and observed mechanics. Next, by evaluating molecular local stiffness, we gain valuable insights into the dynamical heterogeneities of CNC film in quasi-static tension. Finally, porosity analysis and orientation distribution are discussed to provide insights into the underlying mechanism of deformational behaviors of the CNCs. Our simulation results highlight the critical role of density and microstructure in the mechanics and dynamics of CNCs thin film at a fundamental level, paving the way for tailored design of lightweight performance of cellulose-based materials.

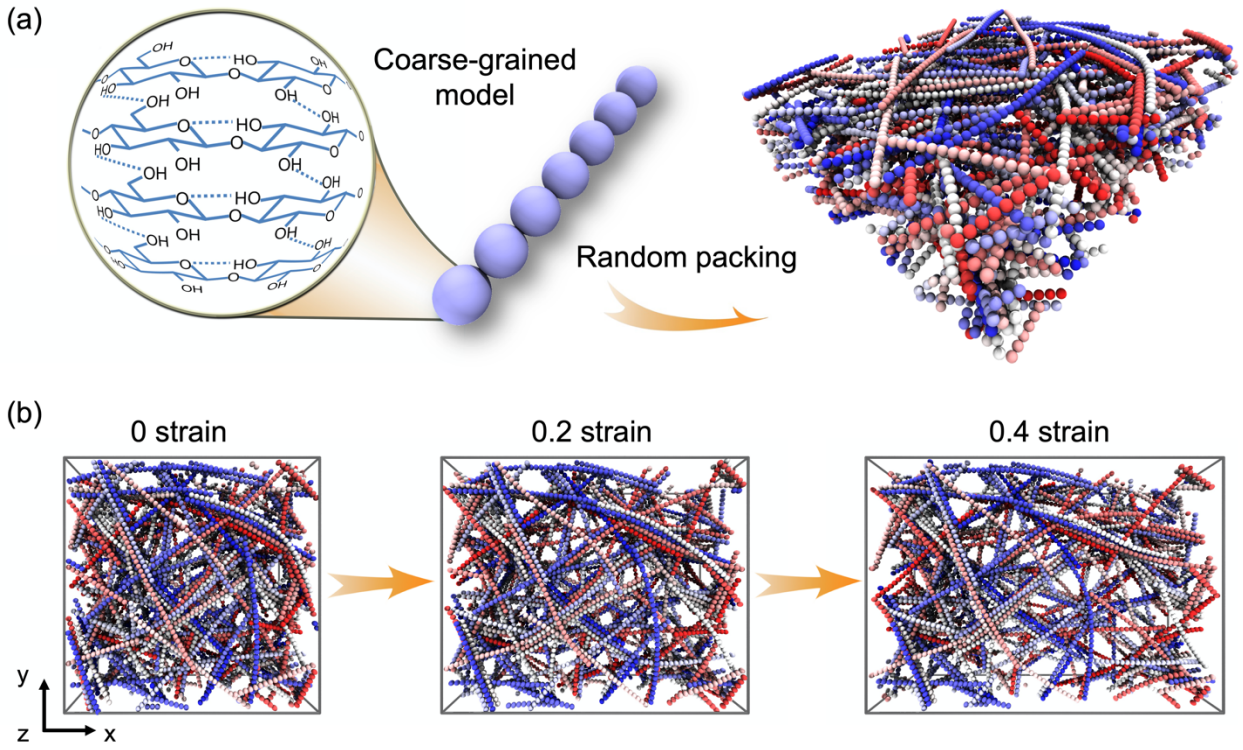

Figure 1. (a) Coarse-graining scheme showing the mapping between molecular-scale cellulose chains (left; shows only the middle four chain) and the corresponding bead-spring CG representation of CNC (middle); the snapshot of the thin film system consisting of randomly oriented CNCs (3D view). (b) The snapshots of the CG thin film under uniaxial tension at different strains (top view).

METHODS

Overview of Coarse-Grained Model of CNCs. The 'bead-spring' mesoscopic CG model of explored CNC thin film system in this study is derived from all-atomistic (AA) counterpart of elementary cellulose fibril with Iβ-crystal structure. Within this model, each CG bead with the radius R = 17 Å corresponds to 3 repeat-unit atoms made of a 36-chain structured (110) cross-section of CNCs as illustrated in **Fig. 1a**. The CG force fields are developed following a strain energy conservation paradigm by conserving the elastic strain energy and matching the mechanical properties of AA CNCs.[40] Specifically, the CG bonded interaction terms, *i.e.*, bonds and angular bending along the fiber axial direction, are captured by harmonic spring potentials; pairwise nonbonded interactions are represented by the Morse potential, where the potential parameters are determined to preserve the interfacial adhesion energy of AA model of CNC. More detailed description of the CG model development can be found in the previous study [40]. Previous studies have shown that this CG model is capable of capturing the elastic, failure properties of nanocellulose to a good approximation and offering a promising scheme for simulating the ballistic impact on both structural and mechanical features of CNC film, in broadly agreement with other simulations and experimental observations [37,56].

All the CG-MD simulations are carried out using LAMMPS software package [57] and the visualization of simulation snapshots is performed by the Visual Molecular Dynamics (VMD).[58] To generate a representative network model, various amount of CNCs with 32 CG beads per CNC (length ~ 100 nm) are randomly packed into a fixed simulation cell with the size of 150 nm × 150 nm × 45 nm, forming the network system with randomly in-plane oriented configurations (**Fig. 1a**). To mimic the thin film systems, periodic boundary conditions (PBCs) are applied in the *x*-*y*

plane while non-PBC is applied in *z*-direction (*i.e.*, the thickness direction); two completely smooth implicit repulsive walls are introduced underneath and above the film for better control of geometry and density of films. The implemented repulsive wall has the following 9-3 Lennard-Jones (LJ) potential function

$$U_w(r_z) = \varepsilon_w \left[\frac{2}{15} \left(\frac{\sigma}{r_z} \right)^9 - \left(\frac{\sigma}{r_z} \right)^3 \right] \qquad r_z < r_c \tag{1}$$

where ε_w refers to the strength parameter (*i.e.*, the depth of potential well) for wall-bead interactions, r_z is the distance of the CG bead from the wall, r_c with a value of 2.5 Å is the cutoff distance at which the CG bead and wall no longer interact. The potential energy of the wall potential is shifted so that the wall-particle interaction energy is zero at the cutoff distance. We also performed additional free-standing film simulations without wall potential by adding extra vacuum space on *z*-direction to create free surfaces on top and bottom, and the result shows that there is no noticeable surface effect on elastic moduli, likely due to the high rigidity of CNC and large porosity of the film (**Fig. S1** in Supporting Information). Moreover, we also test free-standing CNCs thin films with larger thicknesses, and the result shows that the elastic moduli are nearly invariant with film thickness, which again confirms the non-significant free surface effect on the mechanical response (**Fig. S2** in Supporting Information).

During the equilibrium process, the simulated CNC thin film systems first undergo an energy minimization using the iterative conjugate gradient algorithm,[59] followed by two annealing cycles for 20 ns under a canonical ensemble (NVT), where the temperature is elevated from 300 to 1000 K and then cooled backed to 300 K. Afterward, the system is further performed for dynamics equilibration runs at the target density for another 10 ns at 300 K under the NVT ensemble. An integration timestep of Δt = 5 fs is adopted for all CG-MD simulations. Prior to mechanical response, structural stability and equilibration are confirmed by ensuring the total

potential energy convergence is achieved. Six models are generated with independent initial configurations for each system to ensure adequate samplings and determine the averaged properties with standard deviation. The error bar in figures refers to the corresponding standard deviation.

Property calculations. We perform the strain-controlled uniaxial tensile deformation in the *x*-direction for the CNC thin film system. A constant engineering strain rate of 0.05 ns^{-1} is applied for all the simulations, which lies in the range of values adopted in previous simulation studies [40,53,60]. We elaborate in Supporting Information **Fig. S5** that the stress and elastic modulus show an increase with strain rate, which is consistent with previous simulations of various nanomaterials [61]. However, the rate of that increase appears to be lower at small strain rates, indicating that the modulus is approaching nearly constant at lower strain rate values and the adopted rate in this study is close to the rate-independence regime. During the tensile deformation, the dimension in the lateral directions (*i.e.*, both *y*- and *z*-directions) is fixed. The stress component in the tensile direction is determined via the atomic virial stress tensor by[62]

$$\sigma_{xx} = -\frac{1}{V}\left[\sum_{i}^{N} m_i (v_i)_x (v_i)_x + \sum_{i}^{N} (r_i)_x (f_i)_x\right] \quad (2)$$

where V is the volume of the system, N is the total number of CG beads, m_i, v_i, r_i, and f_i refer to the mass, velocity, position, and force vector of the ith bead, respectively.

To quantify the molecular "free volume" and "stiffness" of the CNCs, Debye-Waller factor (DWF) $\langle u^2 \rangle$, a short-time fast dynamics property, is calculated. In our simulations, we calculate $\langle u^2 \rangle$ from the mean-square displacement (MSD) $\langle r^2(t) \rangle$ of the center of mass of CG beads, where $\langle u^2 \rangle$ is defined as the average value of $\langle r^2(t) \rangle$ within the certain range of 1 to 4 ns, corresponding to a caging time scale estimated from our simulations,

$$\langle r^2(t)\rangle = \langle \left| r_j(t) - r_j(0) \right|^2 \rangle \quad (3)$$

where $r_j(t)$ is the position of the center of mass of the j^{th} bead at time t and $\langle ... \rangle$ denotes the ensemble average of all of beads.

The void analysis of the thin films is performed to calculate the pore size distribution (PSD) and maximum pore size using the Zeo++[63,64] open-source package, which is based on the Voronoi cell decomposition to identify probe-accessible domains of void space in a porous material. PSD calculations are performed using a probe of radius set to 1.2 Å.

To evaluate the collective alignment of the in-plane CNCs, orientation order parameter (S) is calculated from the following equation

$$S = \langle \frac{3}{2}\cos^2\phi - \frac{1}{2} \rangle \quad (4)$$

where ϕ is the angle formed by the bond vector connecting two consecutive CG beads relative to the deformation direction, the bracket denotes the ensemble average over all CG bond vectors. Under this definition, the value of S is bounded between -0.5 and 1. S = 1 and -0.5 indicate perfect alignment of all entities along and perpendicular to the stretching direction, respectively. This definition yields S = 0.25 for a random orientation distribution in two-dimensional thin film configuration. To explore the local orientation distribution, we further generalize Eq. (4) for evaluation of local order parameter base on each individual bond vector in the thin film system.

RESULTS AND DISCUSSION

Mechanical properties of CNC network. We begin by characterizing how mechanical response depends on the packing density ρ for CNC thin films. Experimentally, it is commonly observed that neat CNC films with $\rho \sim$ 0.2–0.9 g/cm^3 have typically been produced by solution casting techniques.[65] In the present work, we systematically vary ρ from 0.2 to 0.8 g/cm^3 to generate

CNCs model with different packing density by adjusting the amount of CNCs packed into the simulation cell, correspondingly. It can be seen from **Fig. 1a** that CNC thin film model possesses a web-like structure consisting of a random network of CNCs. We next compare the mechanical response of different packing density film systems to uniaxial tensile loading. **Fig. 1b** shows the representative simulation snapshots of the tensile deformation at a strain of 0, 0.2, and 0.4 in *x*-direction for ρ = 0.4 g/cm^3. It can be observed that as the strain increases, the CNCs become more aligned toward the tensile direction with increased porosity, which will be discussed in detail later. **Fig. 2a** shows the typical stress *vs.* strain outputs of the CNC network with varying ρ. The overall stress-strain response of CNC thin film is qualitatively similar to previous computational studies on CNC-based materials,[40,53,66] where the elastic, yield, and plastic regions can be discerned with the strain increasing. For better comparison, the stress-strain curve of higher density is shifted upwards to the origin. The Young's modulus E is calculated by linearly fitting the stress-strain data up to 1% of strain as plotted via dashed lines. The film system with a larger value of ρ, which consists of more CNCs to undertake the load, thereby exhibits a greater E and tensile strength. It can also be clearly observed that the fluctuation amplitude of stress in the plastic regime becomes larger as ρ increases, resulting from the enhanced interfacial friction between CNCs in closer contact.[53] Previous experimental and computational investigations have also consistently suggested that both the modulus and tensile strength show an increasing trend with density of nanocellulose-based materials with porous structure.[53,70,71]

It should be noted that negative normal stress (NNS) is observed at higher packing density (ρ = 0.8 g/cm^3), where the negative sign indicates that the network is subjected to the compressive prestress. This can be attributed to non-equilibrium state of the network arising from the large bending stiffness of the rod-like CNC and high packing density [67,68]. Moreover, we currently

explore the film systems with uniform CNC length; however, there could be variation in CNC length distribution in the experimentally synthesized films [69]. Introducing variation in CNC or CNF length distribution could likely affect the packing density and porosity of the films and thus reduce the NNS, especially at a larger density, which deserves to be explored in the future work.

Fig. 2b shows a scaling relationship between E and ρ of thin film systems normalized by the property values of individual pristine CNC (*i.e.*, E_s = 134 GPa and ρ_s = 1.63 g/cm^3), respectively. Such relation can be well described by the empirical Gibson and Ashby (GA) model [72] for porous or foam-like systems,

$$\frac{E}{E_s} = C\left(\frac{\rho}{\rho_s}\right)^n \tag{5}$$

where C and n are fitting constants associated with the polymeric geometry and deformation mode of the struts making up the foam, respectively [73]. In particular, n is characterized by values in the range of 1 to 4 based upon the specific microstructures of cellular materials [72]. Here, we estimate n to be about 1.42 for CNC thin film system, which is lower than the reported n = 2.73 for 3D graphene assembly and n = 2 for conventional polymeric open-cell foams,[74] suggesting that the in-plane microstructures of CNC film system are somehow different from those of conventional polymeric foams. Furthermore, larger n value (*i.e.*, $n \approx 2$) has been reported in recent work for bulk CNC network system (*i.e.*, no free surface or interface) under the shear deformation,[53] suggesting that n is likely dependent on the dimensionality of microstructures closely associated with the packing efficiency (*i.e.,* 2D *vs.* 3D packing). Although the underlying mechanisms of the variation of exponent n remains to be further understood, quantifying such power-law scaling between the density ρ and the mechanical property E is particularly useful as it provides a feasible route to predict the mechanical performance of the CNC thin film system.

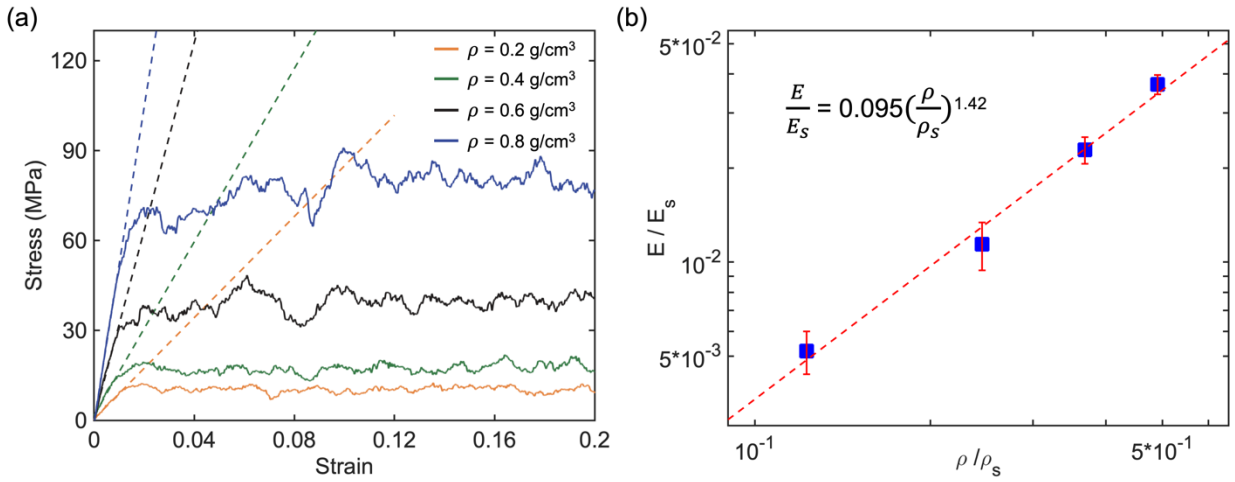

Figure 2. (a) Stress-strain responses for CNC thin film with various packing density (ρ = 0.2, 0.4, 0.6, 0.8 g/cm^3) under uniaxial tension. The dashed lines show the slope of the linear regime within 1% strain, where the Young's modulus E is determined. (b) The normalized Young's modulus of CNC thin film as a function of its mass density, where E_s = 134 GPa and ρ_s = 1.63 g/cm^3 correspond to the Young's modulus and density of individual pristine CNC. The dashed line shows power-law scaling obtained in the study.

Evaluation of molecular stiffness of CNC network. To facilitate a better understanding of the influence of packing density and deformation on the dynamics of CNC thin film, we next examine the Debye-Waller factor $\langle u^2 \rangle$, a fast-dynamics property which quantifies the local "free volume" and inversely related to the molecular "stiffness" of the material [75]. $\langle u^2 \rangle$ is a particularly interesting property as it can be experimentally accessible from both X-ray, neutron, and other scattering measurements [76]. In this present work, we examine the molecular stiffness by evaluating the $1/\langle u^2 \rangle$ for both the overall CNC film system as a whole as well as each CG segment separately. The inset in **Fig. 3** shows the comparison of time-dependent $\langle r^2(t) \rangle$ results for different density ρ, where $\langle u^2 \rangle$ can be obtained as the average value of $\langle r^2(t) \rangle$ over the time period of 1 ~ 4 ns. As ρ increases, a significant decrease in $\langle r^2(t) \rangle$ is observed, indicating that increasing the

packing density leads to a suppressed segmental mobility of CNC thin film. Moreover, an inverse relationship between the modulus of the materials and $\langle u^2 \rangle$ is often observed in the polymer glasses and other glass-forming liquids (*e.g.*, metallic glasses) [75,77], indicating a strong correlation between dynamic vibrations of segments and elastic response of the materials. **Fig. 3** shows the test of the correlation between the Young's modulus E and $1/\langle u^2 \rangle$ for the CNC porous system. Consistent with former observations, we clearly observe that E obeys an apparent linear relationship with $1/\langle u^2 \rangle$ with varying ρ. The observed $1/\langle u^2 \rangle$ value seems to be a 'transferable' measure of local stiffness among various types of microstructures (*i.e.*, condensed materials such as polymer glasses *vs.* porous network), making this an attractive quantity for bottom-up prediction of the mechanical properties of the network materials.

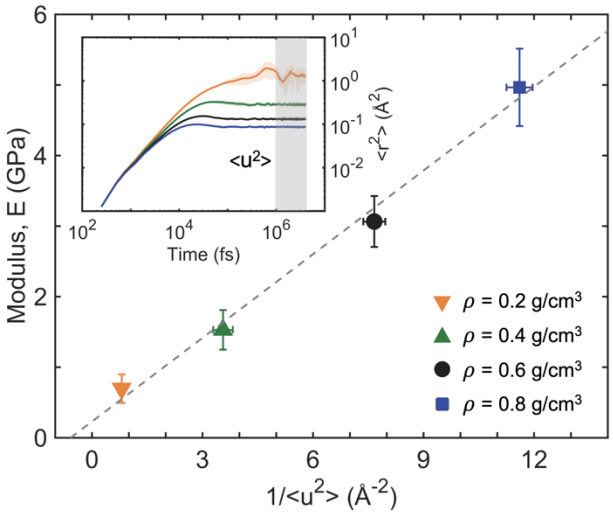

Figure 3. The linear scaling relationship between Young's modulus E and molecular stiffness $1/\langle u^2 \rangle$ of the CNC thin film for different density ρ. (Inset) The MSD $\langle r^2(t) \rangle$ of the center of mass of the CG beads *vs.* t for various ρ. The highlighted gray region marks the time range when $\langle u^2 \rangle$ is obtained from the $\langle r^2(t) \rangle$ measurement.

We next seek to answer whether $1/\langle u^2 \rangle$ can be used to assess deformational response at a molecular level during the tensile process even beyond the elastic regime. To reliably estimate $\langle u^2 \rangle$

during deformation, we further relax the CNC system at each certain strain for additional 4 ns to avoid far out of equilibrium condition. This ensures that the proper equilibration of the CNC system can be achieved before collecting the data for MSD $\langle r^2(t)\rangle$ calculation under the deformation conditions (see the stress relaxation in the deformation in **Fig. S4** in Supporting Information). We consider five representative strains ε, *i.e.*, ε = 0.01, corresponding to low deformation regime where the stress *vs.* strain curve is nearly linear, and ε from 0.1 to 0.4, corresponding to the strain hardening regimes considered in our work. **Fig. 4a** shows segmental $\langle r^2(t)\rangle$ results for CNC film system at different strains during the tensile deformation for a representative initial ρ of 0.4 g/cm^3. Similar to what we observe for the various density (as shown in the inset of **Fig. 3**), we observe a noticeably increase in $\langle r^2(t)\rangle$ as strain ε increases; this indicates that overall segments mobility is enhanced by subjecting the CNC film to a certain deformation.

Fig. 4b summarizes the molecular stiffness $1/\langle u^2\rangle$ results as a function of tensile strain ε for different initial packing density ρ. It can be observed that the $1/\langle u^2\rangle$ decreases with varying ε for all the given ρ tested herein, where the data fall onto the linear scaling relationship for each ρ as marked by the dashed lines. Such influence of ε on $1/\langle u^2\rangle$, however, is more noticeable for CNC thin film with a higher initial ρ. We hypothesize that this trend is due to the fact that as the applied tensile ε gradually enhanced, the local free spaces between CNCs within the porous film system tend to be enlarged, resulting in an increased segmental mobility (*i.e.*, lower molecular stiffness $1/\langle u^2\rangle$). To test this hypothesis, we further plot $1/\langle u^2\rangle$ *vs.* concurrent density ρ_c during the deformation as shown in **Fig. 4c**. Remarkably, all the data can be universally captured by a nearly linear relationship, demonstrating the direct coupling between molecular stiffness and density even during the deformation.

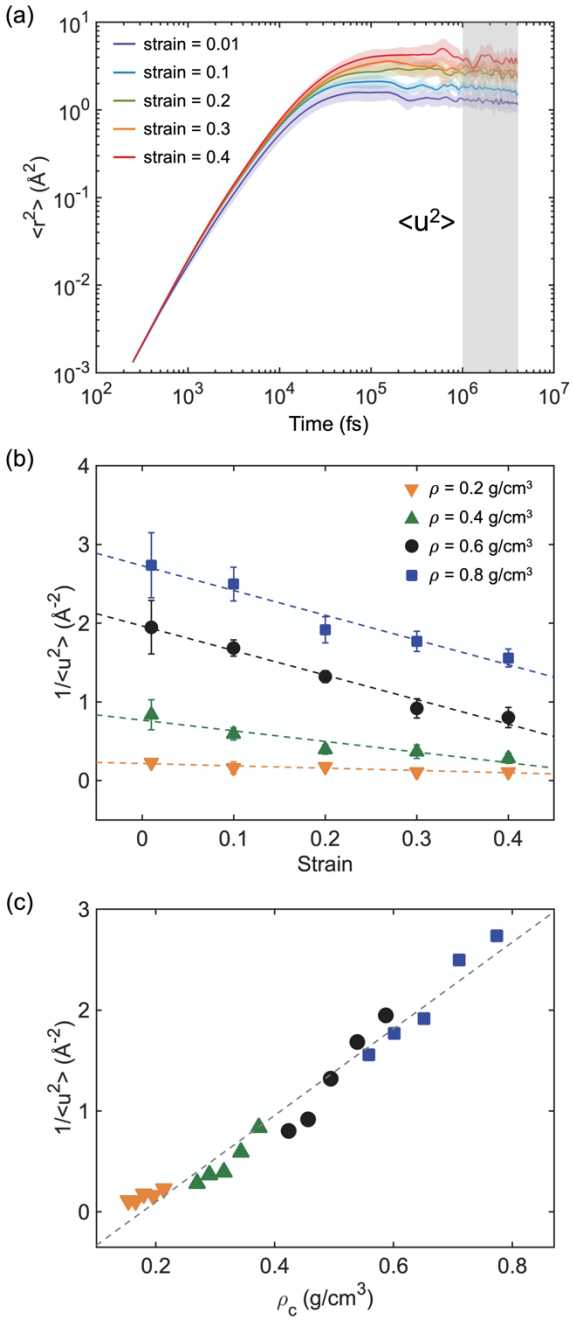

Figure 4. (a) The representative MSD $\langle r^2(t)\rangle$ of the CNCs model with initial ρ of 0.4 g/cm^3 for different strain during the tensile deformation. The highlighted gray region marks the time range when $\langle u^2\rangle$ is obtained from the $\langle r^2(t)\rangle$ measurement. (b) Molecular stiffness $1/\langle u^2\rangle$ *vs.* strain for CNC film with different initial packing density ρ, where a linear relationship is observed. (c)

Universal relationship between the molecular stiffness $1/\langle u^2 \rangle$ and concurrent density ρ_c during the deformation for different initial packing density ρ.

Dynamic heterogeneity of CNC network. To provide fundamental insights into the dynamics of CNCs under deformation, we evaluate the spatial distribution of local molecular stiffness $1/\langle u^2 \rangle$, which serves as a measure of the dynamic heterogeneity in disordered materials. In particular, dynamic heterogeneity has been considered as one of significant characteristic behaviors of glass-forming materials such as polymers, where dynamic clusters of both mobile and immobile segments coexist and interpenetrate each other evolving in time.[77] Previous study based on small-angle X-ray scattering (SAXS) and solid state NMR spectroscopy experiments has also reported the evidence of changes in the nanoscale heterogeneity in molecular mobility and solid structure of cellulose influenced by solvent exchange [78].

We thus examine the local molecular mobility (*i.e.*, stiffness) in CNC thin film model to determine how altering packing density and tensile strain affects this aspect of spatial heterogeneity. The MSD $\langle r^2(t) \rangle$ is then calculated for each individual segment (*i.e.*, CG bead) within the CNC network, and thus enables us to associate the values of $1/\langle u^2 \rangle$ with the mobile and immobile segments for a given configuration. The row images in **Fig. 5a** and **b** show 2D color maps of the local stiffness $1/\langle u^2 \rangle$ distribution for typical configurations at ρ of 0.2 and 0.4 g/cm^3, respectively, where the CNC system is subjected to deformation in x-direction. Note that the blue domains correspond to the segments with a higher local mobility and lower stiffness, while the orange domains correspond to relatively stiff regions of segments with a lower mobility. The amplitude of the fluctuations of local stiffness $1/\langle u^2 \rangle$ is much larger for the higher packing density ρ (note the difference in scale on each colormap comparing **Fig. 5a** and **b**), indicating that the

denser CNC film system becomes more heterogeneous in terms of the local stiffness. CNC network at higher ρ possesses a rather uniform mass distribution (*i.e.*, free voids are reduced), but such system is apparently highly non-uniform at a nanoscale with respect to local mobility and stiffness under deformation. This observation is also analogous to the dynamic behavior of antiplasticized polymer melts – the more efficiently packed antiplasticized polymers exhibit much broader molecular stiffness fluctuations, implying that they are more dynamical heterogeneous than the pure polymers [79]. Another evident feature in the local stiffness distribution is that, during the tensile deformation, the local mobility has been shown to be higher in the regions with larger strain, which can be attributed to the rearrangement and alignment of the CNCs accompanied by increased local free volume and thus the high porosity of the system. It appears that the segments having excessively low mobility (marked in orange) are found in the regions where particles are structurally clustered together, implying that immobile segments are associated with a dense local packing. In contrast, the relatively mobile particles have more interfacial space between CNCs in less dense domains, suggesting that this could translate into the influence by the degree of constrain over the neighboring particles surrounding the segments (the porosity analysis will be discussed in later sections).

Fig. 5c and **d** show the probability distributions of local molecular stiffness $1/\langle u^2 \rangle$ for all segments in our system at ρ of 0.2 and 0.4 g/cm^3, respectively, where we find that the distributions for three typical strains take a form of approximately Gaussian distribution. The difference in the distributions for varying strains is quite dramatic; as strain increases from 0.01 to 0.4, the distribution of $1/\langle u^2 \rangle$ becomes much more concentrated with a relatively narrow range and higher peak intensity, yielding more homogeneity of molecular stiffness within the CNC network. Furthermore, the average value of $1/\langle u^2 \rangle$ is smaller in the CNC system at large strain, and the range

of $1/\langle u^2 \rangle$ fluctuation is also smaller, suggesting the level of dynamic heterogeneity tends to be largely reduced despite the increased porosity within CNC network during the deformation.

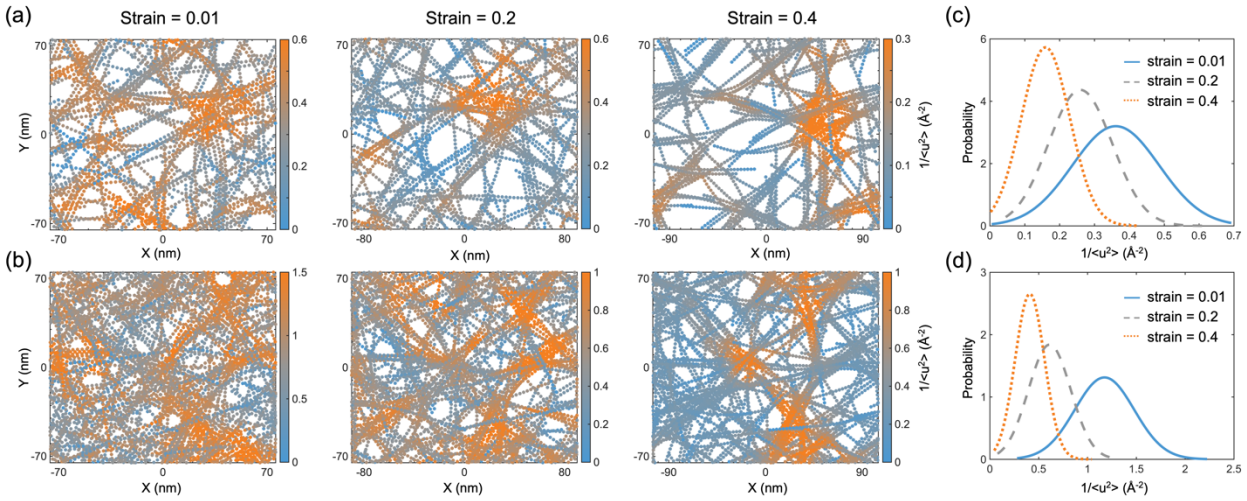

Figure 5. Color maps of local molecular stiffness $1/\langle u^2 \rangle$ distribution of CNC thin film for different tensile strains at (a) ρ = 0.2 g/cm^3 and (b) ρ = 0.4 g/cm^3, respectively. The blue domains correspond to segments with a higher local mobility or lower local stiffness, while orange domains correspond to a lower local mobility or higher local stiffness. Note that the color scale is different in each panel. Probability distribution of $1/\langle u^2 \rangle$ for different tensile strains at (c) ρ = 0.2 g/cm^3 and (d) ρ = 0.4 g/cm^3, respectively.

Porosity of the network. As discussed above, the observed dynamic heterogeneity during the deformation could be well correlated to the degree of geometrical constrains (*i.e.*, the size and distribution of nanopores) within CNC porous network. Here, we examine how the porous structures of CNC network evolves during the uniaxial loading. From the consecutive snapshots shown in the **Fig. 1b**, it can be clearly observed that free voids become notably deformed and, with increasing tensile strain, they tend to coalesce into relatively larger pores. The pore size distribution (PSD) for stretched CNC networks with initial packing densities of ρ = 0.2, 0.4, 0.8

g/cm^3 are presented in **Fig. 6a**. The distribution is narrow at high ρ and it becomes broader as the average packing density decreases, indicating that less dense network structure exhibits substantially more pores and overall free volume (*i.e.*, the volume accessible for the CNCs to occupy) of the films than the corresponding denser system. With further increasing strain for each given density, the peak of PSD curves become smaller and progressively shift toward large value of pore size, corresponding to the enlarged interconnectivity and free voids of CNC network during the extension. Furthermore, **Fig. 6b** summarizes the results of the largest pore diameter (LPD) as a function of strain for different ρ, where a linear growth of LPD with strain is observed for the network system with a given ρ. The formation of largest pore is evident at lower packing density and higher tensile strain, reminiscent of the elongated pore connectivity and coalescence of adjacent voids as shown in **Fig. 5a** and **b**.

The free volume and PSD are important characteristics of the porous network structure, particularly for membrane applications of gas permeability, which governs the gas barrier performance. Using the positron annihilation lifetime spectroscopy (PALS) approach, Nuruddin and coworkers measured the free volume of CNC films with different structural alignments of CNC, emphasizing that shear-aligned CNC films with reduced free volume size exhibit higher gas barrier performance [42]. Chowdhury *et al.* also showed that induction of anisotropy in the CNC films can effectively control the overall free volume of the system associated with the gas diffusion path, resulting in tunable barrier properties in packing applications [41]. On the other hand, the mechanical properties of cellulose films have a strong dependence upon the porosity of network structure. As found in previous experimental studies of cellulose nanopaper, density (as an inverse correlation of porosity) exhibits positive impact on both modulus and strength [71,80].

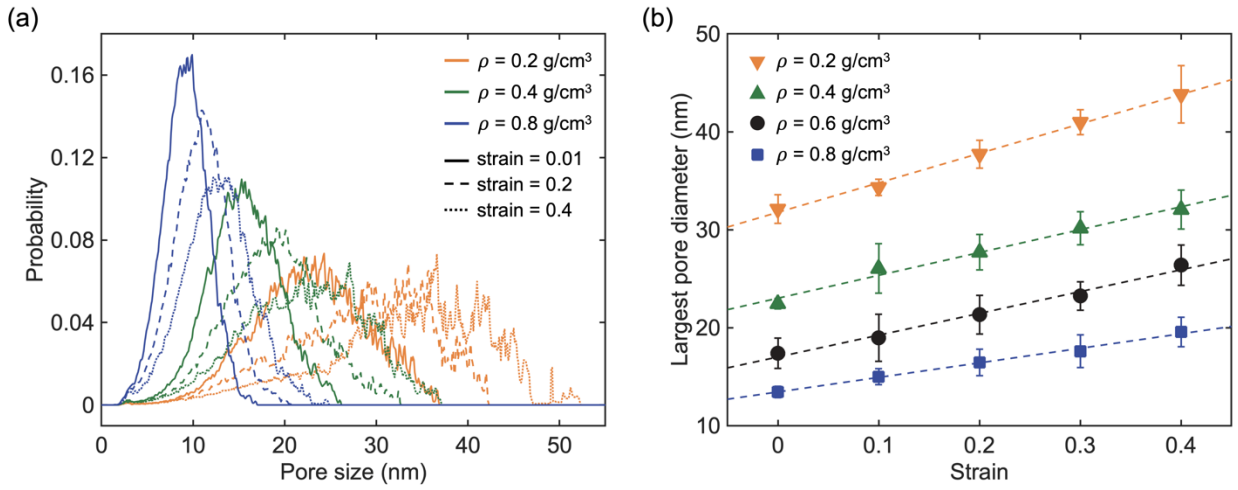

Figure 6. (a) Pore size distributions for CNC network with varying initial packing density ρ at strain of 0.01 (solid curve), 0.2 (dashed curve), and 0.4 (dotted curve). (b) Largest pore size as a function of strain for various ρ, where a linear relationship is observed.

Strain-induced alignment of CNCs. To further understand the strain-induced microstructural change at a nanoscale level, the orientation of CNCs is evaluated by calculating the average order parameter S of the network using Eq. (4). By definition, the relatively large S reflects alignment tendency along the stretching direction, while small S reflects alignment perpendicular to the stretching direction. **Fig. 7a** summarizes the order parameter S as a function of strain under four packing densities ρ from 0.2 to 0.8 g/cm^3. It is observed that the alignment of CNCs increases with strain in a similar fashion for all packing densities considered. S at 0 strain is nearly 0.25 for all densities, indicating randomly orientated CNCs prior to deformation. As the tensile strain increases, the CNCs tend to align in the deformation axis and exhibit a higher order parameter. Another observation is that the S value at each strain is nearly independent of packing density, despite the fact that the network with lower ρ has a higher degree of free volume and thus there is less restriction for CNC self-orientation during deformation.

Next, probability distribution of local order parameter is evaluated to track the detailed CNCs alignment changes upon deformation, where 1 and -0.5 correspond to CNC orientation along and perpendicular to the strain direction, respectively (**Fig. 7b**). Consistently, we find a transition from isotropy to tendency-toward-anisotropy upon stretching; the population of local *S* seen in the intermediate levels of parallel alignment (0.25 ~ 1) increases, while those shown in the intermediate levels of transverse dimension (-0.5 ~ 0.25) decreases with strain. Notably, a bimodal-like distribution is observed at higher strain, where the primary peak gradually increases and shifts to the right, while the secondary peak slightly shifts toward small *S*. This observation indicates CNCs tend to deform and align along the stretching axis, therefore subsequently of higher average orientation, giving rise to greater anisotropy. Such phenomenon has also been experimentally observed [81] and proposed by the recent MD study [82] on the polymers with a higher chain rigidity, where amorphous polymer chains were largely extended and oriented towards the parallel-to-strain direction by increasing the tensile strain. Moreover, strong correlation between alignment and mechanical properties of nanocellulose-based film system has also been proposed in both experiments and simulations [83–89], showing that aligned nanocrystals can largely enhance the modulus and strength in the alignment direction.

Fig. 7c and **d** show the spatial variation of the local order parameter *S* for typical configurations of CNC thin film system, providing the relative intensity level for local *S* changes upon the application of external tensile deformation. Evidently, the phenomenon that CNCs tend to be aligned parallel/perpendicular to the stretching direction is more pronounced at a larger strain, as marked by more red and blue-color domains. In addition, no direct correlation is observed between with the local *S* and local stiffness $1/\langle u^2 \rangle$ (**Fig. S5**, Supporting Information), suggesting

that the particle mobility is more associated with the degree of local packing and density compared to the CNC orientation.

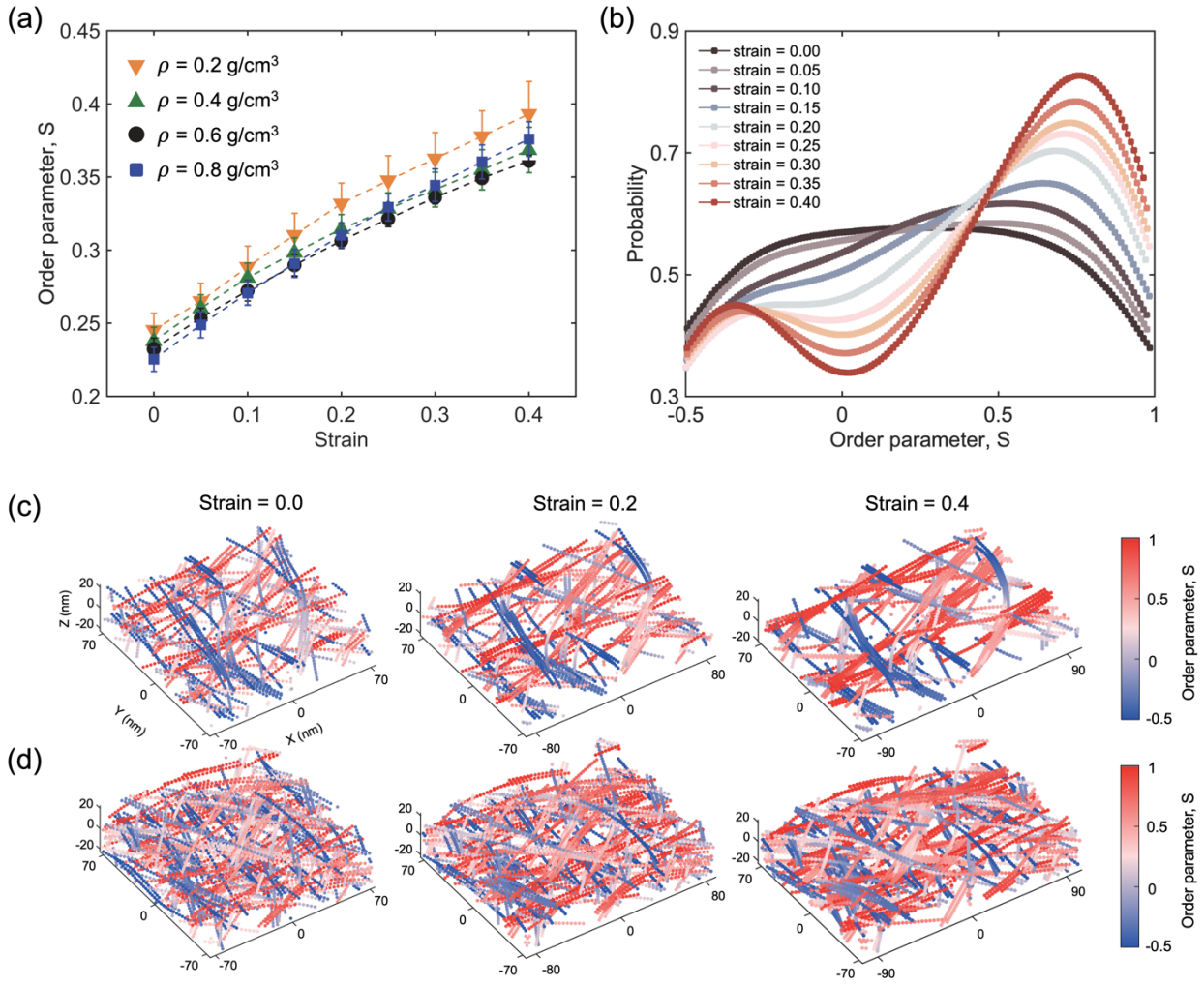

Figure 7. (a) Averaged order parameter *S* of CNCs within the films versus strain at various packing densities ρ. (b) Typical probability distribution of local order parameter *S* of CNC network with varying strains for ρ = 0.2 g/cm^3. Spatial variation of local order parameter *S* of CNC network with varying strain for (c) packing density ρ = 0.2 g/cm^3 and (d) ρ = 0.4 g/cm^3, respectively. The color map scale is the same for all images (color online).

CONCLUSION

In summary, we have systematically investigated the microstructure and dynamics in the deformational behaviors of nanocellulose thin film composed of disoriented CNCs by employing the atomistically informed CG-MD simulations. Specifically, our simulation results show that the Young's modulus *vs.* packing density can be quantitatively predicted by the power-law scaling relationship for the CNC films, which is found to be fundamentally related to the mobility and molecular stiffness of CNCs within the film as quantified by inversed Debye-Waller factor $1/\langle u^2 \rangle$. Analyses of distribution of local $1/\langle u^2 \rangle$ further reveal that CNC thin films with higher density exhibits a higher degree of dynamic heterogeneity, despite a more homogeneous mass distribution; however, such dynamic heterogeneity tends to be suppressed during the tensile process beyond the elastic regime. During the deformation, the randomly oriented CNCs tend to be more aligned towards the stretching direction, accompanied with increased free volume and porosity; the dynamics and molecular stiffness, however, is found to be more associated with the degree of local packing and density allowed for particle motion instead of the CNC orientation. Our work provides valuable insights into the dynamics and microstructural features of CNC films under deformation at a fundamental level, aiding in the tailored design of structural performance of cellulose-based materials.

CONFLICTS OF INTERESTS

There are no conflicts to declare.

ACKNOWLEDGMENTS

Z.L., Y.L. and W.X. acknowledge the support from the National Science Foundation (NSF) under NSF CMMI Award No. 2113558. The authors acknowledge the support from the North Dakota State University (NDSU) Foundation and Alumni Association through the Centennial Endowment Fund. Yida Zhang acknowledges the support of NSF CMMI Award No. 2113474. W.X. acknowledges the support from the North Dakota Established Program to Stimulate Competitive Research (ND EPSCoR) through the New Faculty Award. This work used supercomputing resources of the CCAST at NDSU, which were made possible in part by NSF MRI Award No. 2019077.

REFERENCES

[1] R. Chandra, R. Rustgi, Biodegradable polymers, Prog. Polym. Sci. 23 (1998) 1273–1335.

[2] C.N. Cutter, Opportunities for bio-based packaging technologies to improve the quality and safety of fresh and further processed muscle foods, Meat Sci. 74 (2006) 131–142.

[3] V. Favier, H. Chanzy, J.Y. Cavaillé, Polymer Nanocomposites Reinforced by Cellulose Whiskers, Macromolecules. 28 (1995) 6365–6367.

[4] V. Favier, G.R. Canova, J.Y. Cavaille, ' H Chanzy, ' A Dufresne, C. Gauthie, Polymers for Advanced Technologies Nanocomposite Materials from Latex and Cellulose Whiskers, Polym. Adv. Technol. 6 (1995) 351–355.

[5] S.X. Peng, S. Shrestha, Y. Yoo, J.P. Youngblood, Enhanced dispersion and properties of a two-component epoxy nanocomposite using surface modified cellulose nanocrystals, Polymer (Guildf). 112 (2017) 359–368.

[6] S. Shrestha, R.A. Chowdhury, M.D. Toomey, D. Betancourt, F. Montes, J.P. Youngblood, Surface hydrophobization of TEMPO-oxidized cellulose nanofibrils (CNFs) using a facile, aqueous modification process and its effect on properties of epoxy nanocomposites, Cellulose. 26 (2019) 9631–9643.

[7] H. Zhu, Z. Xiao, D. Liu, Y. Li, N.J. Weadock, Z. Fang, J. Huang, L. Hu, Biodegradable transparent substrates for flexible organic-light-emitting diodes, Energy Environ. Sci. 6 (2013) 2105–2111.

[8] F.A. Müller, L. Müller, I. Hofmann, P. Greil, M.M. Wenzel, R. Staudenmaier, Cellulose-based scaffold materials for cartilage tissue engineering, Biomaterials. 27 (2006) 3955–3963.

[9] A. Svensson, E. Nicklasson, T. Harrah, B. Panilaitis, D.L. Kaplan, M. Brittberg, P. Gatenholm, Bacterial cellulose as a potential scaffold for tissue engineering of cartilage, Biomaterials. 26 (2005) 419–431.

[10] J.P. de Oliveira, G.P. Bruni, S.L.M. el Halal, F.C. Bertoldi, A.R.G. Dias, E. da R. Zavareze, Cellulose nanocrystals from rice and oat husks and their application in aerogels for food packaging, Int. J. Biol. Macromol. 124 (2019) 175–184.

[11] J. Bras, S. Saini, Nanocellulose in functional packaging, Cellul. Nanofibre Compos. Prod. Prop. Appl. 12 (2017) 175–213.

[12] M. Nuruddin, A. Chowdhury, S.A. Haque, M. Rahman, S.F. Farhad, M.S. Jahan, A. Quaiyyum, Extraction and characterization of cellulose microfibrils from agricultural wastes in an integrated biorefinery initiative, Cellul. Chem. Technol. 45 (2011) 347–354.

[13] D. Klemm, D. Schumann, F. Kramer, N. Hebler, D. Koth, B. Sultanova, Nanocellulose materials - Different cellulose, different functionality, Macromol. Symp. 280 (2009) 60–71.

[14] D.M. Fox, R.S. Rodriguez, M.N. Devilbiss, J. Woodcock, C.S. Davis, R. Sinko, S. Keten, J.W. Gilman, Simultaneously Tailoring Surface Energies and Thermal Stabilities of Cellulose Nanocrystals Using Ion Exchange: Effects on Polymer Composite Properties for Transportation, Infrastructure, and Renewable Energy Applications, ACS Appl. Mater. Interfaces. 8 (2016) 27270–27281.

[15] R.J. Moon, A. Martini, J. Nairn, J. Simonsen, J. Youngblood, Cellulose nanomaterials review: structure, properties and nanocomposites., Chem. Soc. Rev. (2011).

[16] M. Nuruddin, M. Hosur, M.J. Uddin, D. Baah, S. Jeelani, A novel approach for extracting cellulose nanofibers from lignocellulosic biomass by ball milling combined with chemical

treatment, J. Appl. Polym. Sci. 133 (2016).
[17] Y. Habibi, L.A. Lucia, O.J. Rojas, Cellulose nanocrystals: Chemistry, self-assembly, and applications, Chem. Rev. (2010).
[18] A. Chakraborty, M. Sain, M. Kortschot, Cellulose microfibrils: A novel method of preparation using high shear refining and cryocrushing, Holzforschung. 59 (2005) 102–107.
[19] S. Wang, Q. Cheng, A novel process to isolate fibrils from cellulose fibers by high-intensity ultrasonication, part 1: Process optimization, J. Appl. Polym. Sci. 113 (2009) 1270–1275.
[20] T. Zimmermann, N. Bordeanu, E. Strub, Properties of nanofibrillated cellulose from different raw materials and its reinforcement potential, Carbohydr. Polym. 79 (2010) 1086–1093.
[21] X. Xu, F. Liu, L. Jiang, J.Y. Zhu, D. Haagenson, D.P. Wiesenborn, Cellulose nanocrystals vs. Cellulose nanofibrils: A comparative study on their microstructures and effects as polymer reinforcing agents, ACS Appl. Mater. Interfaces. 5 (2013) 2999–3009.
[22] X. Xu, H. Wang, L. Jiang, X. Wang, S.A. Payne, J.Y. Zhu, R. Li, Comparison between cellulose nanocrystal and cellulose nanofibril reinforced poly(ethylene oxide) nanofibers and their novel shish-kebab-like crystalline structures, Macromolecules. 47 (2014) 3409–3416.
[23] H. Kargarzadeh, M. Mariano, J. Huang, N. Lin, I. Ahmad, A. Dufresne, S. Thomas, Recent developments on nanocellulose reinforced polymer nanocomposites: A review, Polymer (Guildf). 132 (2017) 368–393.
[24] J.A. Diaz, X. Wu, A. Martini, J.P. Youngblood, R.J. Moon, Thermal expansion of self-organized and shear-oriented cellulose nanocrystal films, Biomacromolecules. 14 (2013) 2900–2908.
[25] M. Iguchi;, S. Yamanaka;, A. Budhiono;, Bacterial cellulose - a masterpiece of nature's arts, J. Mater. Sci. 35 (2000) 261–270.
[26] R. Sinko, X. Qin, S. Keten, Interfacial mechanics of cellulose nanocrystals, MRS Bull. (2015).
[27] C.D. Edgar, D.G. Gray, Smooth model cellulose I surfaces from nanocrystal suspensions, Cellulose. 10 (2003) 299–306.
[28] Y. Habibi, I. Hoeger, S.S. Kelley, O.J. Rojas, Development of Langmuir - Schaeffer cellulose nanocrystal monolayers and their interfacial behaviors, Langmuir. 26 (2010) 990–1001.
[29] Y. Habibi, L. Foulon, V. Aguié-Béghin, M. Molinari, R. Douillard, Langmuir-Blodgett films of cellulose nanocrystals: Preparation and characterization, J. Colloid Interface Sci. 316 (2007) 388–397.
[30] H. Sehaqui, N. Ezekiel Mushi, S. Morimune, M. Salajkova, T. Nishino, L.A. Berglund, Cellulose nanofiber orientation in nanopaper and nanocomposites by cold drawing, ACS Appl. Mater. Interfaces. 4 (2012) 1043–1049.
[31] M. Nogi, S. Iwamoto, A.N. Nakagaito, H. Yano, Optically Transparent Nanofiber Paper, Adv. Mater. (2009).
[32] A.J. Svagan, M.A.S.A. Samir, L.A. Berglund, Biomimetic foams of high mechanical performance based on nanostructured cell walls reinforced by native cellulose nanofibrils, Adv. Mater. 20 (2008) 1263–1269.
[33] Y. Habibi, T. Heim, R. Douillard, AC electric field-assisted assembly and alignment of

cellulose nanocrystals, J. Polym. Sci. Part B Polym. Phys. 46 (2008) 1430–1436.
[34] W. Gindl, G. Emsenhuber, G. Maier, J. Keckes, Cellulose in never-dried gel oriented by an AC electric field, Biomacromolecules. 10 (2009) 1315–1318.
[35] I. Kvien, K. Oksman, Orientation of cellulose nanowhiskers in polyvinyl alcohol, Appl. Phys. A Mater. Sci. Process. 87 (2007) 641–643.
[36] W.J. Orts, L. Godbout, R.H. Marchessault, J.F. Revol, Enhanced ordering of liquid crystalline suspensions of cellulose microfibrils: A small angle neutron scattering study, Macromolecules. 31 (1998) 5717–5725.
[37] X. Qin, B.C. Marchi, Z. Meng, S. Keten, Impact resistance of nanocellulose films with bioinspired Bouligand microstructures, Nanoscale Adv. 1 (2019) 1351–1361.
[38] Y. Bouligand, Twisted fibrous arrangements in biological materials and cholesteric mesophases, Tissue Cell. 4 (1972) 189–217.
[39] K.E. Shopsowitz, A. Stahl, W.Y. Hamad, M.J. MacLachlan, Hard templating of nanocrystalline titanium dioxide with chiral nematic ordering, Angew. Chemie - Int. Ed. 51 (2012) 6886–6890.
[40] X. Qin, S. Feng, Z. Meng, S. Keten, Optimizing the mechanical properties of cellulose nanopaper through surface energy and critical length scale considerations, Cellulose. 24 (2017) 3289–3299.
[41] R.A. Chowdhury, M. Nuruddin, C. Clarkson, F. Montes, J. Howarter, J.P. Youngblood, Cellulose Nanocrystal (CNC) Coatings with Controlled Anisotropy as High-Performance Gas Barrier Films, ACS Appl. Mater. Interfaces. 11 (2019) 1376–1383.
[42] M. Nuruddin, R.A. Chowdhury, N. Lopez-Perez, F.J. Montes, J.P. Youngblood, J.A. Howarter, Influence of Free Volume Determined by Positron Annihilation Lifetime Spectroscopy (PALS) on Gas Permeability of Cellulose Nanocrystal Films, ACS Appl. Mater. Interfaces. 12 (2020) 24380–24389.
[43] A. Kulachenko, T. Denoyelle, S. Galland, S.B. Lindström, Elastic properties of cellulose nanopaper, Cellulose. 19 (2012) 793–807.
[44] S. Goutianos, R. Mao, T. Peijs, Effect of inter-fibre bonding on the fracture of fibrous networks with strong interactions, Int. J. Solids Struct. 136–137 (2018) 271–278.
[45] Q. Meng, B. Li, T. Li, X.Q. Feng, Effects of nanofiber orientations on the fracture toughness of cellulose nanopaper, Eng. Fract. Mech. 194 (2018) 350–361.
[46] K. Kulasinski, R. Guyer, S. Keten, D. Derome, J. Carmeliet, Impact of moisture adsorption on structure and physical properties of amorphous biopolymers, Macromolecules. (2015).
[47] R. Sinko, S. Keten, Traction-separation laws and stick-slip shear phenomenon of interfaces between cellulose nanocrystals, J. Mech. Phys. Solids. 78 (2015) 526–539.
[48] R. Sinko, S. Keten, Effect of moisture on the traction-separation behavior of cellulose nanocrystal interfaces, Appl. Phys. Lett. 105 (2014).
[49] R. Sinko, S. Mishra, L. Ruiz, N. Brandis, S. Keten, Dimensions of biological cellulose nanocrystals maximize fracture strength, ACS Macro Lett. (2014).
[50] H. Zhu, S. Zhu, Z. Jia, S. Parvinian, Y. Li, O. Vaaland, L. Hu, T. Li, Anomalous scaling law of strength and toughness of cellulose nanopaper, Proc. Natl. Acad. Sci. U. S. A. 112 (2015) 8971–8976.
[51] B.C. Marchi, S. Keten, Microstructure and size effects on the mechanics of two dimensional, high aspect ratio nanoparticle assemblies, Front. Mater. 6 (2019) 1–14.
[52] B. Natarajan, A. Krishnamurthy, X. Qin, C.D. Emiroglu, A. Forster, E.J. Foster, C.

Weder, D.M. Fox, S. Keten, J. Obrzut, J.W. Gilman, Binary Cellulose Nanocrystal Blends for Bioinspired Damage Tolerant Photonic Films, Adv. Funct. Mater. 28 (2018) 1–11.
[53] Z. Li, W. Xia, Coarse-grained modeling of nanocellulose network towards understanding the mechanical performance, Extrem. Mech. Lett. 40 (2020).
[54] M. Shishehbor, P.D. Zavattieri, Effects of interface properties on the mechanical properties of bio-inspired cellulose nanocrystal (CNC)-based materials, J. Mech. Phys. Solids. 124 (2019) 871–896.
[55] U. Ray, Z. Pang, T. Li, Mechanics of cellulose nanopaper using a scalable coarse-grained modeling scheme, Cellulose. 0123456789 (2021).
[56] B. Natarajan, A. Krishnamurthy, X. Qin, C.D. Emiroglu, A. Forster, E.J. Foster, C. Weder, D.M. Fox, S. Keten, J. Obrzut, J.W. Gilman, Binary Cellulose Nanocrystal Blends for Bioinspired Damage Tolerant Photonic Films, Adv. Funct. Mater. (2018).
[57] S. Plimpton, Fast parallel algorithms for short-range molecular dynamics, J. Comput. Phys. 117 (1995) 1–19.
[58] W. Humphrey, A. Dalke, K. Schulten, VMD: Visual molecular dynamics, J. Mol. Graph. (1996).
[59] Y. Liao, Z. Li, Fatima, W. Xia, Size-dependent structural behaviors of crumpled graphene sheets, Carbon N. Y. 174 (2021) 148–157.
[60] W. Xia, F. Vargas-Lara, S. Keten, J.F. Douglas, Structure and Dynamics of a Graphene Melt, ACS Nano. 12 (2018) 5427–5435.
[61] A.D. Mulliken, M.C. Boyce, Mechanics of the rate-dependent elastic-plastic deformation of glassy polymers from low to high strain rates, Int. J. Solids Struct. 43 (2006) 1331–1356.
[62] A.P. Thompson, S.J. Plimpton, W. Mattson, General formulation of pressure and stress tensor for arbitrary many-body interaction potentials under periodic boundary conditions, J. Chem. Phys. 131 (2009).
[63] T.F. Willems, C.H. Rycroft, M. Kazi, J.C. Meza, M. Haranczyk, Algorithms and tools for high-throughput geometry-based analysis of crystalline porous materials, Microporous Mesoporous Mater. 149 (2012) 134–141.
[64] R.L. Martin, B. Smit, M. Haranczyk, Addressing challenges of identifying geometrically diverse sets of crystalline porous materials, J. Chem. Inf. Model. 52 (2012) 308–318.
[65] R.J. Moon, A. Martini, J. Nairn, J. Simonsen, J. Youngblood, Cellulose nanomaterials review: Structure, properties and nanocomposites, 2011.
[66] M. Shishehbor, P.D. Zavattieri, Effects of interface properties on the mechanical properties of bio-inspired cellulose nanocrystal (CNC)-based materials, J. Mech. Phys. Solids. 124 (2019) 871–896.
[67] P.A. Janmey, M.E. McCormick, S. Rammensee, J.L. Leight, P.C. Georges, F.C. MacKintosh, Negative normal stress in semiflexible biopolymer gels, Nat. Mater. 6 (2007) 48–51.
[68] E. Conti, F.C. MacKintosh, Cross-linked networks of stiff filaments exhibit negative normal stress, Phys. Rev. Lett. 102 (2009) 1–4.
[69] H. Fukuzumi, T. Saito, A. Isogai, Influence of TEMPO-oxidized cellulose nanofibril length on film properties, Carbohydr. Polym. 93 (2013) 172–177.
[70] H. Sehaqui, T. Zimmermann, P. Tingaut, Hydrophobic cellulose nanopaper through a mild esterification procedure, Cellulose. 21 (2014) 367–382.
[71] M. Henriksson, L.A. Berglund, P. Isaksson, T. Lindström, T. Nishino, Cellulose

nanopaper structures of high toughness, Biomacromolecules. (2008).
[72] L.J. Gibson, M.F. Ashby, The Mechanics of Three-Dimensional Cellular Materials, Proc. R. Soc. A Math. Phys. Eng. Sci. (1982).
[73] O.M. Istrate, B. Chen, Relative modulus-relative density relationships in low density polymer-clay nanocomposite foams, Soft Matter. (2011).
[74] Z. Qin, G.S. Jung, M.J. Kang, M.J. Buehler, The mechanics and design of a lightweight three-dimensional graphene assembly, Sci. Adv. (2017).
[75] B.A. Pazmiño Betancourt, P.Z. Hanakata, F.W. Starr, J.F. Douglas, Quantitative relations between cooperative motion, emergent elasticity, and free volume in model glass-forming polymer materials, Proc. Natl. Acad. Sci. U. S. A. 112 (2015) 2966–2971.
[76] M.C. Bellissent-Funel, A. Filabozzi, S.H. Chen, Measurement of coherent debye-waller factor in in vivo deuterated C- phycocyanin by inelastic neutron scattering, Biophys. J. (1997).
[77] J.F. Douglas, B.A.P. Betancourt, X. Tong, H. Zhang, Localization model description of diffusion and structural relaxation in glass-forming Cu-Zr alloys, J. Stat. Mech. Theory Exp. 2016 (2016) 54048.
[78] D. Ishii, D. Tatsumi, T. Matsumoto, Effect of solvent exchange on the supramolecular structure, the molecular mobility and the dissolution behavior of cellulose in LiCl/DMAc, Carbohydr. Res. 343 (2008) 919–928.
[79] R.A. Riggleman, J.F. Douglas, J.J. De Pablo, Tuning polymer melt fragility with antiplasticizer additives, J. Chem. Phys. 126 (2007).
[80] M. Jonoobi, A.P. Mathew, K. Oksman, Producing low-cost cellulose nanofiber from sludge as new source of raw materials, Ind. Crops Prod. 40 (2012) 232–238.
[81] S. Zhang, A. Alesadi, G.T. Mason, K.L. Chen, G. Freychet, L. Galuska, Y.H. Cheng, P.B.J. St. Onge, M.U. Ocheje, G. Ma, Z. Qian, S. Dhakal, Z. Ahmad, C. Wang, Y.C. Chiu, S. Rondeau-Gagné, W. Xia, X. Gu, Molecular Origin of Strain-Induced Chain Alignment in PDPP-Based Semiconducting Polymeric Thin Films, Adv. Funct. Mater. 2100161 (2021) 1–15.
[82] S.E. Root, S. Savagatrup, C.J. Pais, G. Arya, D.J. Lipomi, Predicting the Mechanical Properties of Organic Semiconductors Using Coarse-Grained Molecular Dynamics Simulations, Macromolecules. 49 (2016) 2886–2894.
[83] M. Shishehbor, M.R. Pouranian, Tuning the mechanical and adhesion properties of carbon nanotubes using aligned cellulose wrap (Cellulose nanotube): A molecular dynamics study, Nanomaterials. 10 (2020).
[84] H. Zhu, S. Zhu, Z. Jia, S. Parvinian, Y. Li, O. Vaaland, L. Hu, T. Li, Anomalous scaling law of strength and toughness of cellulose nanopaper, Proc. Natl. Acad. Sci. U. S. A. (2015).
[85] H. Sehaqui, N. Ezekiel Mushi, S. Morimune, M. Salajkova, T. Nishino, L.A. Berglund, Cellulose nanofiber orientation in nanopaper and nanocomposites by cold drawing, ACS Appl. Mater. Interfaces. (2012).
[86] K.M.O. Håkansson, A.B. Fall, F. Lundell, S. Yu, C. Krywka, S. V. Roth, G. Santoro, M. Kvick, L. Prahl Wittberg, L. Wågberg, L.D. Söderberg, Hydrodynamic alignment and assembly of nanofibrils resulting in strong cellulose filaments, Nat. Commun. 5 (2014).
[87] A.B. Reising, R.J. Moon, J.P. Youngblood, Effect of particle alignment on mechanical properties of neat cellulose nanocrystal films, J-For. 2 (2012) 32–41.
[88] Q. Meng, B. Li, T. Li, X.Q. Feng, Effects of nanofiber orientations on the fracture

toughness of cellulose nanopaper, Eng. Fract. Mech. 194 (2018) 350–361.
[89] M. Shishehbor, H. Son, M. Nuruddin, J.P. Youngblood, C. Davis, P.D. Zavattieri, Influence of alignment and microstructure features on the mechanical properties and failure mechanisms of cellulose nanocrystals (CNC) films, J. Mech. Behav. Biomed. Mater. 118 (2021) 104399.

Supplementary Information for

Microstructure and Dynamics of Nanocellulose Films: Insights into the Deformational Behavior

Zhaofan Li [a], Yangchao Liao [a], Yao Zhang [b], Yida Zhang [c], Wenjie Xia [a, d, *]

[a] *Department of Civil, Construction and Environmental Engineering, North Dakota State University, Fargo, ND 58108, United States*

[b] *Department of Biology, Pennsylvania State University, University Park, PA 16802, United States*

[c] *Department of Civil, Environmental and Architectural Engineering, University of Colorado Boulder, Boulder, CO 80309, United States*

[d] *Materials and Nanotechnology, North Dakota State University, Fargo, ND 58108, United States*

*Corresponding Author. Email: wenjie.xia@ndsu.edu

This file includes:

Figure S1 – S2

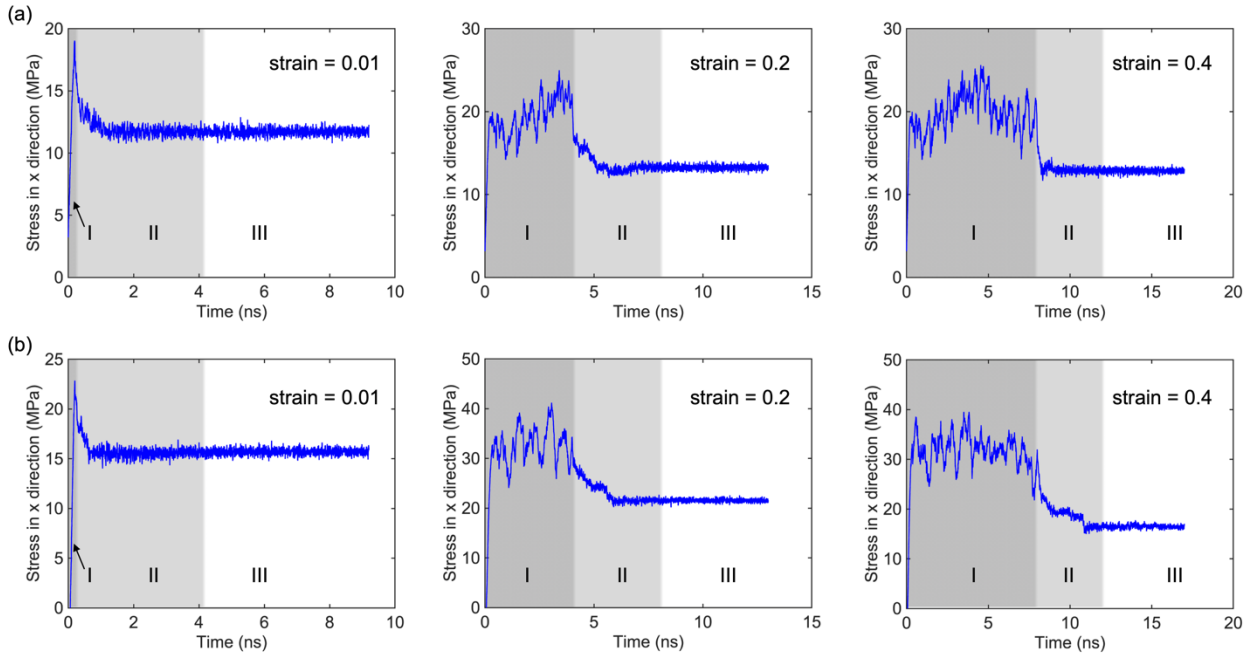

Figure S1. The representative stress relaxation of the CNCs film for different strain during the tensile deformation. Networks have an initial packing density of 0.4 g/cm^3 in panel (a) and a density of 0.6 g/cm^3 in panel (b). Regime I refer to the tensile process. To reliably estimate $\langle u^2 \rangle$ during deformation, the CNC system is further relaxed at each certain strain for additional 4 ns to avoid far out of equilibrium condition shown in the regime II, where the stress decay and convergence is achieved. Subsequently, the data for MSD $\langle r^2(t) \rangle$ calculation is collected at regime III under the deformation conditions.

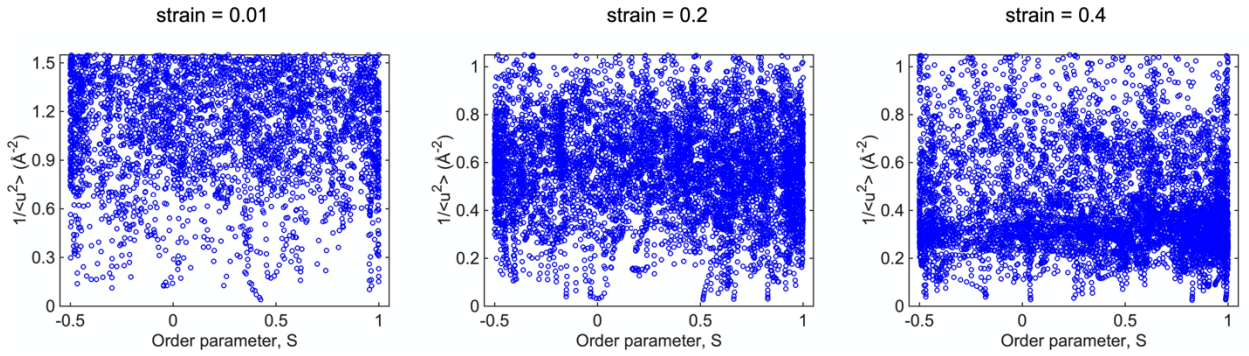

Figure S2. Local stiffness $1/\langle u^2 \rangle$ vs. local order parameter S of CNCs film with initial density of 0.4 g/cm^3 for different strain during the tensile deformation. This analysis verifies that there is no direct correlation between local $1/\langle u^2 \rangle$ and local S within CNCs film system.